Angular Sampling of a Monochromatic, Wide-Field-of-View Camera to Augment Next-Generation Earth Radiation Budget Satellite Observations

Jake J. Gristey[1,2,3], K. Sebastian Schmidt[3,4], Hong Chen[3], Daniel R. Feldman[5], Bruce C. Kindel[3], Joshua Mauss[3,4], Mathew van den Heever[3,4], Maria Z. Hakuba[6], Peter Pilewskie[3]

[1]Cooperative Institute for Research in Environmental Sciences, University of Colorado, Boulder, CO, USA
[2]NOAA Chemical Sciences Laboratory, Boulder, CO, USA
[3]Laboratory for Atmospheric and Space Physics, University of Colorado, Boulder, CO, USA
[4]Department of Atmospheric and Oceanic Sciences, University of Colorado, Boulder, CO, USA
[5]Earth and Environmental Sciences Area, Lawrence Berkeley National Laboratory, Berkeley, CA, USA
[6]NASA Jet Propulsion Laboratory, California Institute of Technology, Pasadena, CA, USA

Correspondence to: Jake J. Gristey (Jake.J.Gristey@noaa.gov)

Abstract. Earth radiation budget (ERB) satellite observations require conversion of the measured radiance, which is a remotely-sensed quantity, to a derived irradiance, which is the relevant energy balance quantity routinely used in modelling and analysis of the climate system. The state-of-the-art approach for radiance-to-irradiance conversion taken by the Clouds and the Earth's Radiant Energy System (CERES) benefits from the exhaustive sampling of radiance anisotropy by multiple CERES instruments across many years. Unfortunately, the CERES approach is not easily extended to new ERB spectral channels that lack previous sampling, such as the "split-shortwave" planned to be part of the next-generation ERB mission Libera. As an alternative approach, the capability of a monochromatic, wide-field-of-view camera to provide dense angular sampling in a much shorter timeframe is assessed. We present a general concept for how this can be achieved and quantify the proficiency of a camera to provide rapid angular distribution model (ADM) generation for the new Libera ultraviolet-and-visible (VIS) sub-band. A single mid-visible camera wavelength (555 nm) is shown to be ideal for representing the VIS sub-band, requiring only basic scene stratification for 555 nm to VIS conversion. Synthetic camera sampling with realistic operating constraints also demonstrates that the angular radiance field of various scenes can be well populated within a single day of sampling, a notable advance over existing approaches. These results provide a path for generating observationally-based VIS ADMs with minimal lag time following Libera's launch. Coupled with efforts to utilize a camera for scene identification, this may also pave the way for future ERB satellite systems to develop stand-alone irradiance products for arbitrary sets of spectral channels, opening up new measurement and science possibilities.

1 Introduction

Satellite observations of the Earth Radiation Budget (ERB) are essential for monitoring Earth's climate because they track the amount of energy available to the Earth system. Consequently, they have been a mainstay from the dawn of the

satellite era through to the present day (Harries et al., 2005; Kandel et al., 1998; Wielicki et al., 1996; Kyle et al., 1993; Barkstrom, 1984; Jacobowitz et al., 1984; Raschke et al., 1973; Vonder Haar and Suomi, 1971; Raschke and Bandeen, 1970). A persistent challenge associated with ERB observations is the conversion of the measured radiance – a quantity dependant on the angle at which a scene is viewed, to a derived irradiance – a quantity that encompasses all view angles. This radiance-to-irradiance conversion is particularly crucial in the shortwave (SW) where strong anisotropy is common, resulting from the surface bi-directional reflectance and the optical properties of the atmosphere including those of absorbing gases, particles, and condensates. The irradiance is far more relevant for Earth system energetics, and therefore it is the derived irradiance products, rather than the direct radiance observations, that are most useful to quantify climate forcing and feedbacks (e.g., Ceppi and Nowack, 2021; Cesana and del Genio, 2021; Kramer et al., 2021; Myers et al., 2021; Raghuraman et al., 2021), constrain and improve climate models (e.g., Hartmann and Ceppi, 2014; Tett et al., 2013b, a; Forster and Gregory, 2006), and inform ERB assessments and scientific understanding (Loeb and Wielicki, 2015; Wild et al., 2015; Stephens et al., 2012; Trenberth, 2009; Vonder Haar and Suomi, 1971).

The solution to the radiance-to-irradiance conversion challenge is provided by so-called angular distribution models (ADMs). These models consist of a set of anisotropic factors, R, to convert the satellite-measured radiance, I, to an irradiance F:

$$F_{s,i} = \frac{\pi I_{s,i,j,k}}{R_{s,i,j,k}}, \tag{1}$$

where the subscript s represents the dependence on scene composition, and the subscripts i, j, k represent the angular dependences on solar zenith angle (SZA), viewing zenith angle (VZA), and relative azimuth angle (RAA), respectively. A full derivation of SW ADMs and discussion of their intricacies was recently outlined in a review article (Gristey et al., 2021). Here, it suffices to recognize that while the perfect ADM would require perfect knowledge of the properties of a given scene, ADMs are often parameterized into discrete scene types and solar-viewing geometries, and that these dimensions are highly stratified in current ERB products from the Clouds and the Earth's Radiant Energy System (CERES) (Su et al., 2015a; Loeb et al., 2005, 2003a). It has been shown that the higher stratification in CERES SW ADMs leads to reduced uncertainty in irradiance products at local and regional scales (Su et al., 2015b; Loeb et al., 2007, 2003b). This approach is made possible by both the retrieval of detailed scene properties using co-flying imager observations and direct sampling of radiance anisotropy accumulated over many years from multiple CERES instruments. The direct sampling of SW radiance anisotropy has largely been achieved through the operation of CERES instruments in rotating azimuth plane scan (RAPS) mode, where the instrument scans in elevation as it rotates in azimuth.

NASA's next-generation ERB satellite mission Libera, which is supported as the first Earth Venture Continuity mission and is due to launch in 2027, will provide continuity to the CERES data record. In addition to hosting heritage spectral channels for continuity, Libera will also host a "split-SW" radiometer to derive separately ultraviolet-to-visible (VIS; 0.3–0.7 μm) and near-infrared (NIR; 0.7–5.0 μm) sub-band irradiances. While detailed spectral information is typically needed to retrieve specific atmospheric properties (e.g., to separate between water vapor and cloud absorptions), the split-SW will

65 bring new science advances by probing how SW energy is partitioned at the surface and in the atmosphere (Hakuba et al., 2022; Carlson et al., 2019; Collins et al., 2006). However, there exists two challenges with applying the state-of-the-art CERES approach for radiance-to-irradiance conversion of Libera split-SW observations. First, the existing CERES SW ADMs cannot be directly applied because the surface and atmospheric absorption, reflection, and scattering differ markedly between the total SW and split-SW. Second, the extensive angular sampling required to generate new split-SW ADMs does

70 not yet exist. While Libera will have the capability to operate in RAPS mode and will co-fly with the Visible Infrared Imaging Radiometer Suite (VIIRS), it is expected to operate primarily in cross-track scan mode to meet continuity requirements; RAPS mode is only anticipated to be available for 12–36 days per year, and will be limited to a finite number of RAPS scans that is expected to be substantially less than the CERES instruments. Implementing highly stratified ADMs for the new split-SW sub-bands following the CERES SW ADM approach is therefore simply not feasible, especially since

75 the development of VIS and NIR irradiance products cannot wait for years to exhaustively sample radiance anisotropy with Libera in RAPS mode.

To address the absence of sufficient angular sampling in the split-SW sub-bands, Libera plans to fly a monochromatic wide-field-of-view (WFOV) camera as part of its instrument package. The camera will continuously take images of the entire Earth disk from horizon-to-horizon with sub-kilometre pixel spacing at nadir, providing dense angular sampling of the

80 radiance field. Uniformity in the camera pixel radiances across the WFOV, expected to be within 1.5% for the Libera camera, will be essential to derive anisotropic factors as in Equation 1. However, the camera radiances are not bound by similarly stringent requirements on absolute accuracy, expected to be within 5%, because the anisotropic factors are calculated as a ratio of radiances in different directions, making a camera appropriate for this task. A camera also provides several other potentially useful sampling opportunities for ERB, such as continuous imaging of the radiometer footprint for

85 rudimentary scene identification, multi-angle views to aid cloud detection and cloud tomography retrieval, and detailed angular radiance variations of a given scene for ADM validation. While the exact specifications of the Libera camera are being actively refined and will be documented in a separate technical paper, we apply several aspects of the expected performance of the Libera camera as realistic constraints during this study.

The purpose of this study is to outline the concept and quantify the capability of a monochromatic WFOV camera to

90 produce VIS ADMs. We focus on the VIS sub-band for reasons outlined in Section 4, but note that the NIR irradiance can subsequently be determined via subtraction of the derived VIS irradiance from the total SW irradiance. An overview of the process is shown in the flow diagram in Figure 1 and proceeds as follows. First, since anticipated data rate constraints dictate that entire camera images are unlikely to be downlinked during the Libera mission, we develop pixel masks that extract a small subset of camera image pixels to meet ADM development needs. Section 3 outlines the choice of pixel masks to

95 provide monochromatic radiances at the radiometer footprint scale across a wide range of viewing angles. One can reasonably question how *monochromatic* (single channel) camera observations translate to *VIS* ADMs, and in Section 4 we show that a mid-visible wavelength provides a very tight relationship with the VIS sub-band requiring only minimal stratification, thereby enabling a spectral conversion that is required to use monochromatic observations to generate VIS

ADMs. In Section 5, we quantify the capability of the camera to provide dense angular sampling needed for ADMs by
100   simulating synthetic camera samples and determining how they would populate the angular space of various scene types.
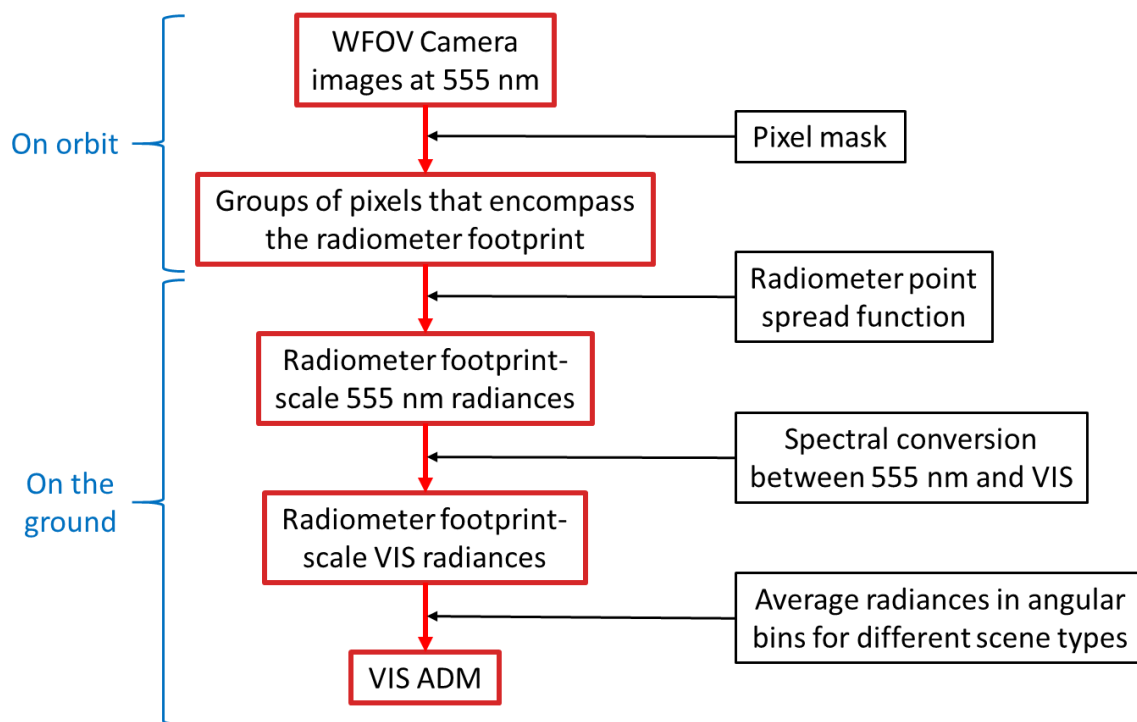
Figure 1. Flow diagram providing a broad overview of the processing steps required to go from WFOV camera images at a single mid-visible wavelength to a VIS sub-band ADM.

2 Data

105   To assess the spectral relationship between a monochromatic camera wavelength and the split-SW bands (Section 4) we
employ multiple datasets. First and primarily, we assess spectral relationships with the Climate Absolute Radiance and
Refractivity Observatory (CLARREO; Wielicki et al., 2013) observing system simulation experiment (OSSE; Feldman et al.,
2015, 2011a, b). The CLARREO OSSE is based on radiative transfer calculations using the MODerate resolution
atmospheric TRANsmission (MODTRAN; Berk et al., 2014) computer code with input atmospheric profiles from climate
110   models, providing a global perspective. Here, we use top-of-atmosphere (TOA) outgoing SW spectral radiances obtained
with profiles from the Commonwealth Scientific and Industrial Research Organisation (CSIRO) climate model output. There
exist a couple of important limitations of the CLARREO OSSE in the context of the present study including limited spectral
and angular resolution in the input surface spectral Bidirectional Reflectance Distribution Function (BRDF), and the fact that
the spectral radiances are only output at nadir. These limitations are addressed with additional observations and simulations,
115   summarized together with all other datasets used in this study in Table 1.

For an observational perspective, we compare the CLARREO OSSE with satellite observations from the Scanning Imaging Absorption Spectrometer for Atmospheric Chartography (SCIAMACHY; Gottwald and Bovensmann, 2011) and aircraft observations from the Airborne Visible Infrared Imaging Spectrometer (AVIRIS; Green et al., 1998). Since the SCIAMACHY data volume is large, and extensive SCIAMACHY observations are not required for this study, we arbitrarily
120 use data from 1st August 2004. We also use "SCIAMACHY-like" simulations over West Africa in 2010 (Gristey and Chiu, 2022; Gristey et al., 2019) that were generated via the Havemann-Taylor Fast Radiative Transfer Code (HT-FRTC; Havemann et al., 2018). A distinct observational perspective is provided by AVIRIS, where we select just four scenes that are frequently encountered across the globe. While limited in global representativeness, these AVIRIS scenes provide a valuable consistency check against the CLARREO OSSE, and have some advantages over SCIAMACHY such as covering a
125 larger fraction of the incoming solar spectrum with much finer spatial resolution enabling better physical interpretation.

To provide some initial insights into the solar-viewing geometry dependence of spectral relationships, we also analyze a dataset of MODTRAN calculations that was used for CERES radiance unfiltering (Loeb et al., 2001). This dataset includes almost 5000 TOA spectral radiances at SZAs, VZAs, and RAAs that are most-often varied simultaneously from one calculation to the next. Since the angular resolution of this CERES unfiltering dataset is still relatively coarse, we further
130 explore detailed angular variations for a given scene by running radiative transfer calculations with libRadtran (Emde et al., 2016; Mayer and Kylling, 2005) using a wrapper code included within the Education and Research 3D Radiative Transfer Toolbox (EaR³T; Chen et al., 2022). This diverse set of radiative transfer calculations and observations helps ensure that our analyses are minimally susceptible to radiative transfer model errors and existing observational limitations.

To assess the angular sampling of various scene types that a WFOV camera could observe (Section 5), we use an
135 intermediate dataset that is applied in the production of CERES Single Scanner Footprint (SSF) data products (Loeb et al., 2003a) called "Cookie Dough". This dataset contains a swath of retrieved geophysical variables (Minnis et al., 2021; Trepte et al., 2019) along the orbit and at the spatial resolution of the spectral imager that is co-flying on the same satellite as a given CERES instrument. In CERES processing, CERES radiometer footprints are then matched to this dataset and applied as a "cookie cutter" to extract the footprint scene properties, hence the colloquial analogy. Specifically, we use Cookie
140 Dough derived from the VIIRS imager on the NOAA-20 satellite for 4 days spread evenly throughout an annual cycle. While a large number of retrieved geophysical variables are available in the dataset, we only extract those that are of most importance for exploring the scene stratification of VIS ADMs: surface type, cloud fraction, and cloud optical depth.

Table 1. Datasets used in this study. Unless otherwise stated, no sub-setting of scene properties is applied.

Name	Key characteristics for this study	Reference(s)
CLARREO OSSE	• Based on radiative transfer with MODTRAN version 5.3.1 • Input profiles from CSIRO climate model output arbitrarily for January 2040 run under the representative concentration pathway 8.5 scenario • Data on a global grid with 96 latitude × 192 longitude points • Output is TOA nadir radiance at 5 nm spectral resolution	(Feldman et al., 2015, 2011a, b)

SCIAMACHY observations	• SW hyperspectral imaging spectrometer that flew on the European Space Agency's Environmental Satellite from 2002–2012 • Reflected solar spectrum from 240–1750 nm, version 8. • Spectral resolution between 0.22 and 1.48 nm depending on spectral region • Data extracted for 1st August 2004, consisting of 24,971 spectra	(Gottwald and Bovensmann, 2011)
SCIAMACHY-like simulations	• Based on radiative transfer with HT-FRTC • 90,917 input profiles derived from A-Train satellite retrievals in 2010 • West Africa only (20°W–20°E and 0°–30°N) • TOA nadir radiance at native SCIAMACHY spectral resolution	(Gristey and Chiu, 2022; Gristey et al., 2019)
AVIRIS observations	• Downward-pointing SW hyperspectral imaging spectrometer flown on the ER-2 aircraft at approximately 20 km altitude • Reflected solar spectrum from 366–2500 nm • Spectral resolution of 10 nm • Data extracted for 4 arbitrary scenes: marine cirrus, marine stratus, cropland, and mixed forest/cumulus clouds.	(Green et al., 1998)
CERES unfiltering simulations	• Based on radiative transfer with MODTRAN version 3.7 • A total of 4956 simulations categorized as land (2520), cloudy ocean (336), clear ocean (588), deep convective cloud (252), and snow (1260), which excludes the highest SZA bin from (Loeb et al., 2001) • Output is TOA radiance at a spectral resolution of 20 cm^{-1} in intervals of 10 cm^{-1} • SZA, VZA, and RAA most-often varied simultaneously from one simulation to the next	(Loeb et al., 2001)
libRadtran simulations	• Single scene: cloud from 0.5–1 km with optical depth of 10, effective radius of 12 microns, and a Lambertian ocean surface with albedo of 0.03 • Fixed SZA of 60° • Fixed VZA of 45° • Variable RAA from 0–360° every 5°	(Chen et al., 2022; Emde et al., 2016; Mayer and Kylling, 2005)
CERES Cookie Dough	• Retrievals from VIIRS on NOAA 20 • Data from 1st January, 1st April, 1st July, and 1st October 2021 • Retrieved variables: surface type, cloud fraction, cloud optical depth • Sub-setting is applied in the Cookie Dough processing by using every eighth VIIRS imager pixel and every other scan line	(Minnis et al., 2021; Trepte et al., 2019)

3 Sub-setting of camera images for dense angular sampling

145  Continuously capturing high-resolution images of the entire Earth disk viewable from satellite altitude creates significant demands on satellite data storage and downlink. For example, the 2048 × 2048 12-bit camera images anticipated every 5 seconds during the Libera mission, shown schematically in Figure 2, equates to a data rate greater than 10,000 kbit/s, which is orders of magnitude larger than the allocation when Libera was proposed. To address this challenge, we recognize that entire images are not necessarily required to meet angular sampling needs for ADM generation. Instead, it is possible to

150  extract a small subset of the overall pixels in each image that encompass a variety of viewing geometries, and only

save/downlink those pixels. These subsets of pixels can be selected by carefully designing and applying pre-designed pixel masks to camera images.
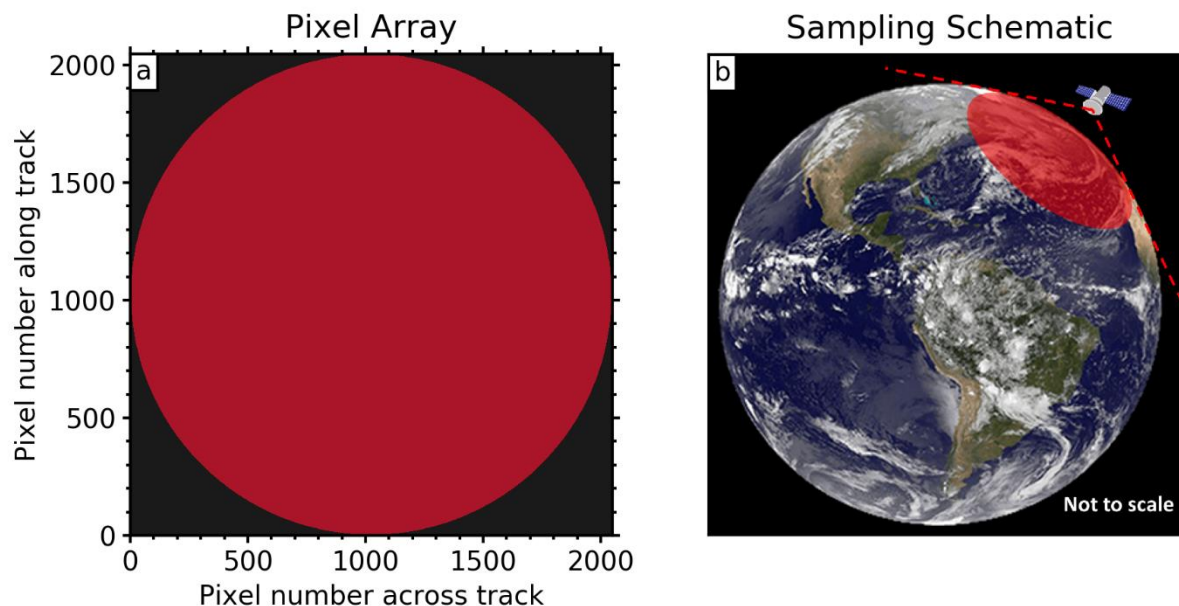
Figure 2. (a) A 2048 × 2048 camera pixel array providing 750 m resolution at nadir (red pixels are viewing Earth while black
155 **pixels fall beyond the horizon) and (b) an instantaneous sampling schematic of a WFOV camera viewing Earth (footprint in red**
shading). This design is broadly consistent with the camera proposed to fly as part of the Libera instrument package at an
estimated altitude of 824 km. (Earth image credit: NASA).

To ensure a pixel mask provides dense angular sampling needed for ADM generation, we structure it around the angular bins applied for SW ADMs from the CERES instrument on the Tropical Rainfall Measuring Mission (TRMM) (henceforth

160 "CERES-TRMM"; Loeb et al., 2003a). These consist of SZA and VZA bins with 10° width and RAA bins with 20° width. While other angular bin definitions could be considered, sampling each of these angular bins at each camera exposure provides a reasonable balance of dense angular sampling while drastically decreasing data rate. The sampling can also be scaled as needed (see below), so the approach is largely insensitive to the initial angular bins used as a reference.

We propose a nominal sampling pattern that consists of separate groups of pixels (henceforth "ADM samples") at the

165 center of every CERES-TRMM angular bin for each camera exposure (Figure 3a and b). In this case, only 79,218/4,194,304 (1.89%) of the pixels in each image are extracted. One implication of this fixed nominal pixel mask is that identical VZAs are sampled from one camera exposure to the next. Since the angular distribution of reflected solar radiation can be non-linear within angular bins, samples taken at the center of an angular bin may not be representative of that angular bin as a whole. To address this issue, the location of the ADM sample can be randomized within each angular bin on orbit (e.g.,

170 Figure 3c and d). Randomization can be implemented from one camera exposure to the next, or updated periodically, so long as the net result does not lead to sampling bias within angular bins. Note that the geolocated ADM samples (e.g., Figure 3b and d) experience significant stretching with increasing VZA resulting from a combination of three factors: the view angle

projection onto a flat surface, the additional curvature of the Earth, and a further additional distortion from the "fish-eye" camera lens.
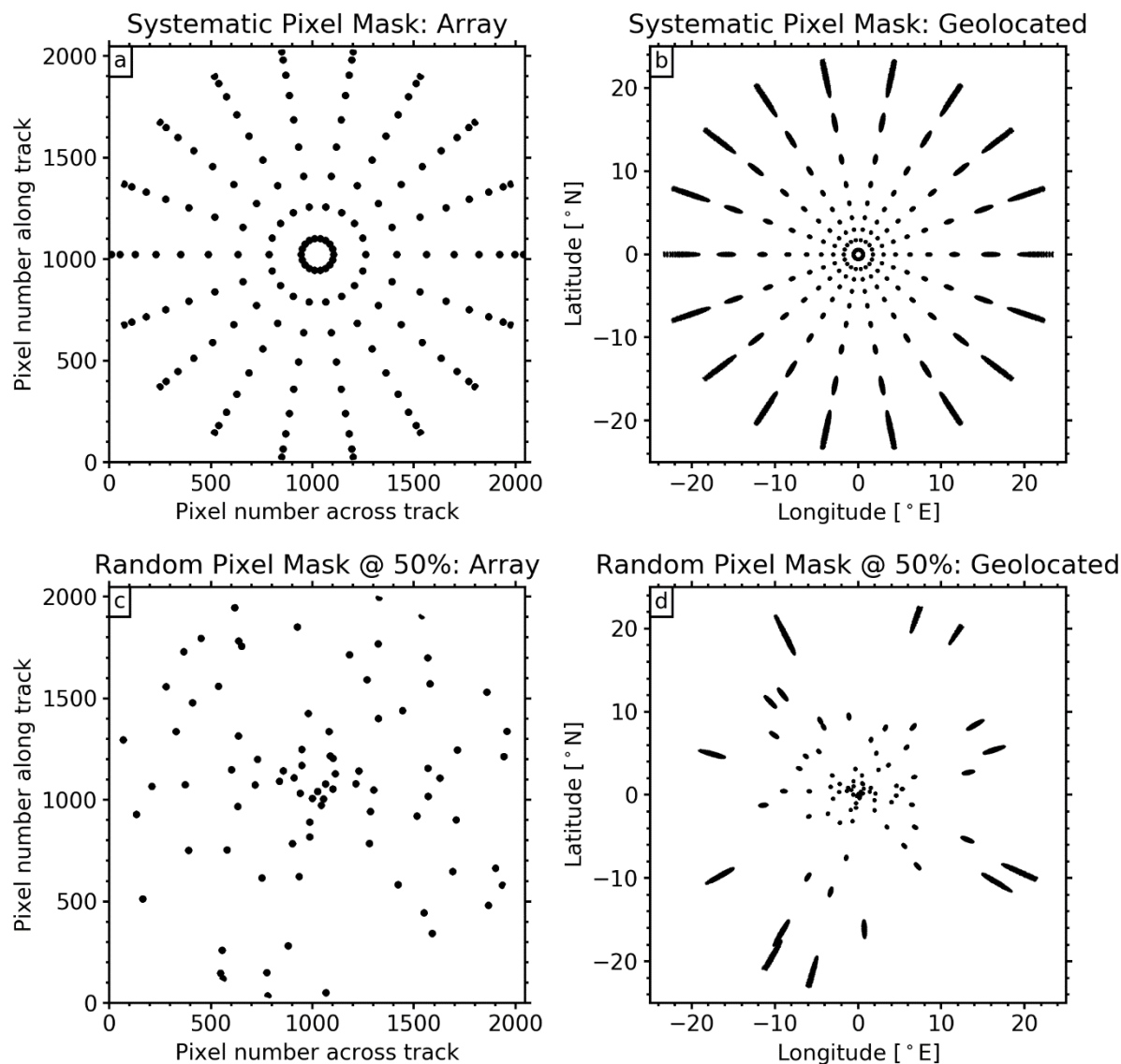
Figure 3. Preliminary camera pixel masks to provide dense angular sampling while limiting downlink data rate. A systematic camera pixel mask (a and b) consists of groups of pixels ("ADM samples") at the centre of each CERES-TRMM angular bin, while a randomized camera pixel mask with a scaling factor of 50% (c and d) consists of half of the total number of ADM samples randomly located across and within CERES-TRMM angular bins. Data are plotted in two coordinate systems: the camera pixel array (a and c) and geo-located nominally at the equator and prime meridian (b and d). Note that pixels within an ADM sample that fall beyond the horizon are not shown.

Given that it is not strictly necessary to sample every VZA and RAA bin per camera exposure to generate ADMs, an important flexibility of this pixel mask is the ability to implement a scaling factor to adjust the number of ADM samples for

each camera exposure. This enables tailoring to a given bandwidth/data rate. For the example given in Figure 3c and d, a
scaling factor of 50% is applied, leading to a pixel mask where only 50% of the angular bins contain an ADM sample at each
camera exposure, equivalent to only 39,609/4,194,304 (0.94%) of the pixels in each image. The selection of which angular
bins are sampled can also be randomized to avoid sampling biases over an extended time period. A 50% scaling factor with
randomization from one exposure to the next is applied in the simulation experiments in Section 5.

Each ADM sample within a pixel mask contains almost 500 pixels that are selected to encompass the radiometer
footprint of approximately 20 km in diameter. Camera pixel-level radiances can then be weighted by the radiometer point
spread function (PSF). The purpose of this is to ensure that the spatial resolution of the sampling is consistent for the
radiances that are used to generate ADMs, and the radiances that will utilize ADMs which will come from the split-SW
radiometer. When comparing to the actual PSF of the CERES radiometer that is planned to be identical for Libera (Figure 4),
it is clear that some non-negligible contributions to the equivalent radiometer measurement would originate outside the
ADM sample. The size of the ADM sample can easily be increased as needed and should not influence the results of this
study, but note that this situation at nadir represents a worst-case scenario since the actual coverage of the radiometer PSF
increases with VZA due to the additional camera lens distortion not experienced by the radiometers.
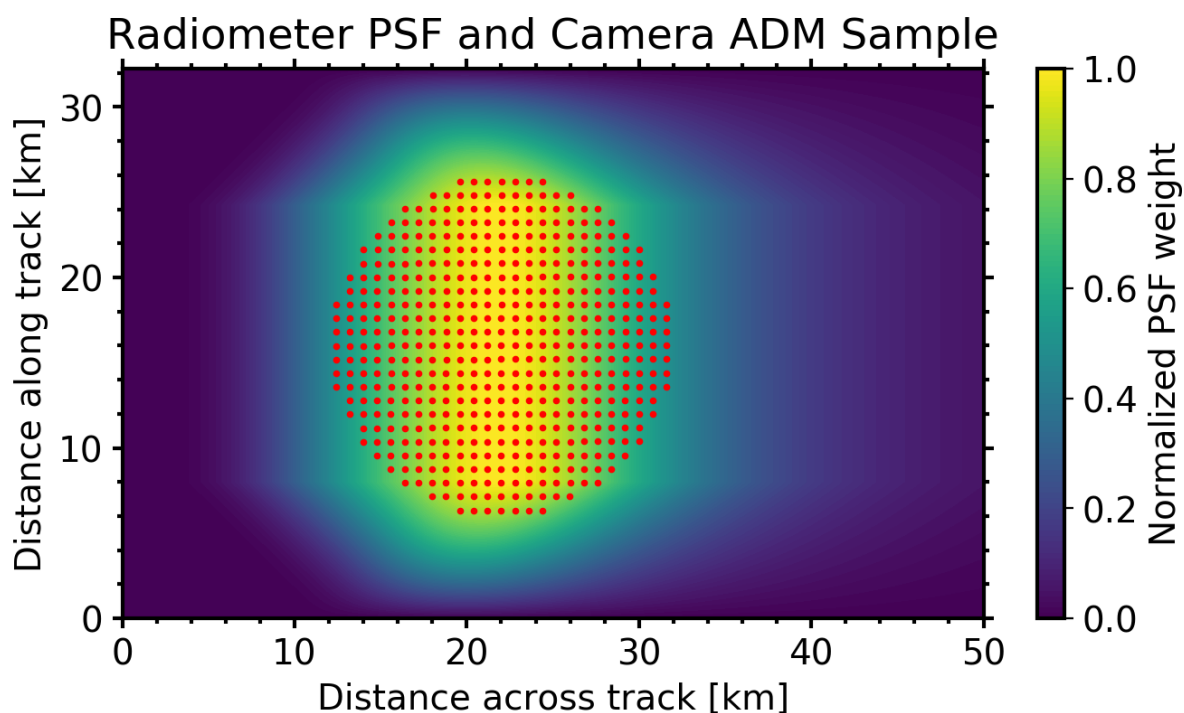
Figure 4. Near-nadir comparison between the CERES (and expected Libera) point spread function (PSF) normalized to a maximum value of 1 (background contours) and the individual pixels constituting an ADM sample from the WFOV camera (red dots).

4 Choice of camera wavelength

Application of monochromatic angular radiances to generate broadband ADMs is inspired partly by Corbett and Su (2015) who found that, of the Multi-angle Imaging SpectroRadiometer (MISR; Diner et al., 1998) spectral channels, the 865 nm channel correlates best with the CERES total SW, and subsequently incorporated radiances from this MISR channel to create CERES SW ADMs over Antarctic sastrugi. To determine the applicability of a similar spectral conversion to aid the generation of split-SW ADMs, we examine a variety of independent datasets containing spectrally-resolved reflected SW radiances. For a given wavelength to act as a good proxy for one of the split-SW sub-bands, a very high correlation between them should exist. That way, the measured radiance in the monochromatic channel can serve as a predictor for radiance across the spectral channel of interest. Note that this implies a conversion from monochromatic radiances to broad-band radiances to inform broad-band ADMs, and therefore does not directly concern monochromatic ADMs.

The CLARREO OSSE that includes scenes across the entire globe (Figure 5a) suggests that, while 865 nm is amongst the highest correlations for the NIR sub-band, it is not an optimal proxy for either of the split-SW bands. The primary reasons for this lower correlation are that water vapor, liquid, and ice absorption, and surface bi-directional reflectance, all affect the NIR sub-band strongly, vary significantly across scene type, and produce spectrally-varying impacts across the NIR sub-band (discussed further below; see Figure 7). Instead, we find that the highest correlation occurs between mid-visible wavelengths and the VIS sub-band, where absorption is minimal and surface bi-directional reflectance has less spectral dependence. These high VIS sub-band correlations are broadly consistent with results from SCIAMACHY observations and SCIAMACHY-like simulations (Figure 5b). Some differences are expected given that the CLARREO OSSE is based on global gridded data, while the SCIAMACHY observations are only extracted for a single day exhibiting denser sampling in polar regions, and the SCIAMACHY-like simulations are for an entire year but only over a limited region (see details in Section 2). Despite the different characteristics of the datasets, the consistently high correlation at mid-visible wavelengths provides reassurance that the result is robust. Although a range of mid-visible wavelengths exists where similarly high correlations occur, we proceed specifically with 555 nm because it is expected to have several operational advantages for the Libera mission. These include matching the VIIRS M4 band due to co-fly with Libera that will be useful for consistency checks and flat-fielding activities (not discussed here), and 555 nm is at the longer-wavelength end of the highest correlations, which is important to minimize on-orbit optical degradation that occurs preferentially at shorter wavelengths (Béland et al., 2014).
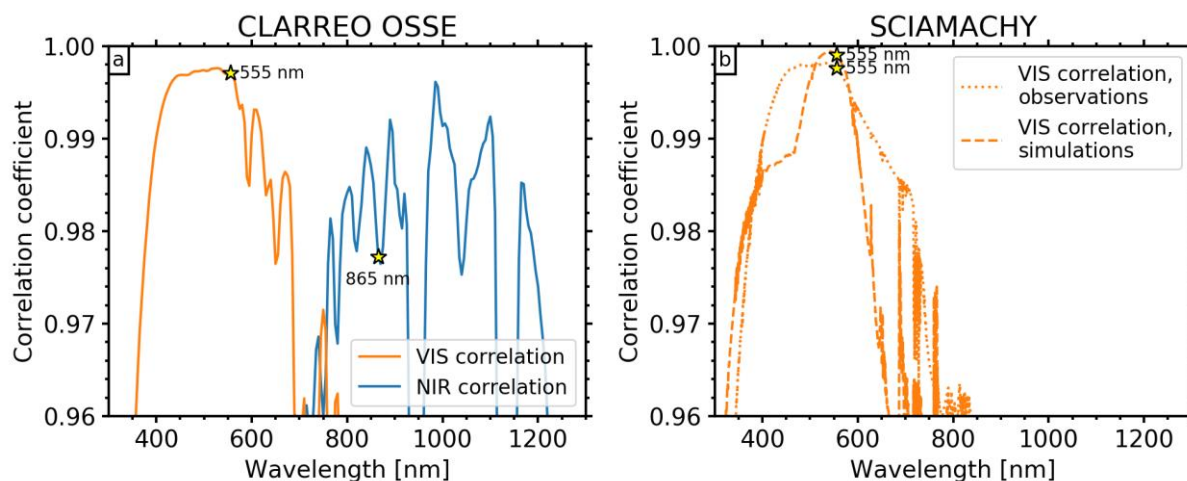
Figure 5. Pearson correlation coefficient between TOA spectral radiances and the VIS (orange) and NIR (blue) sub-band radiances for (a) all scenes in the CLARREO OSSE and (b) SCIAMACHY observations and SCIAMACHY-like simulations. Star symbols highlight the wavelengths of focus: 555 nm and 865 nm. Correlations extend beyond the given vertical axis range, but only the highest correlations are shown. Note that the NIR sub-band correlation is not shown for SCIAMACHY because of spectrally-incomplete data in the NIR.

As an additional test of the spectral relationships determined from the CLARREO OSSE and SCIAMACHY data (Figure 5), selected AVIRIS scenes are examined (Figure 6), this time with the full dynamic range of correlations retained to reveal the spectral character of the individual scenes. The AVIRIS correlation spectra largely tell the same story; mid-visible wavelengths consistently exhibit the highest correlation with the VIS sub-band. The NIR sub-band correlation, however, varies substantially more between these scenes for any given wavelength. When clouds dominate the scene (Figure 6a and b), the VIS and NIR sub-band correlations are themselves correlated given the generally high reflectance of clouds throughout the spectrum. In contrast, when vegetation dominates the scene (Figure 6c and d), the VIS and NIR correlations are themselves anti-correlated, with a sharp transition at the so-called near-infrared edge where vegetation is typically dark in the visible and becomes much brighter in the NIR. For the cloud-free agriculture scene (Figure 6c), there is even a negative correlation between the VIS sub-band and NIR wavelengths from around 700–1200 nm. The correlation spectra closely mimic (or are the inverse of) typical surface or cloud reflectance spectra, demonstrating the dominance of the underlying surface or cloud spectral reflectance for the VIS or NIR sub-band correlation. Regardless of these spectral details, 555 nm maintains a very high correlation with the VIS sub-band across all scenes, around 0.99 or greater.
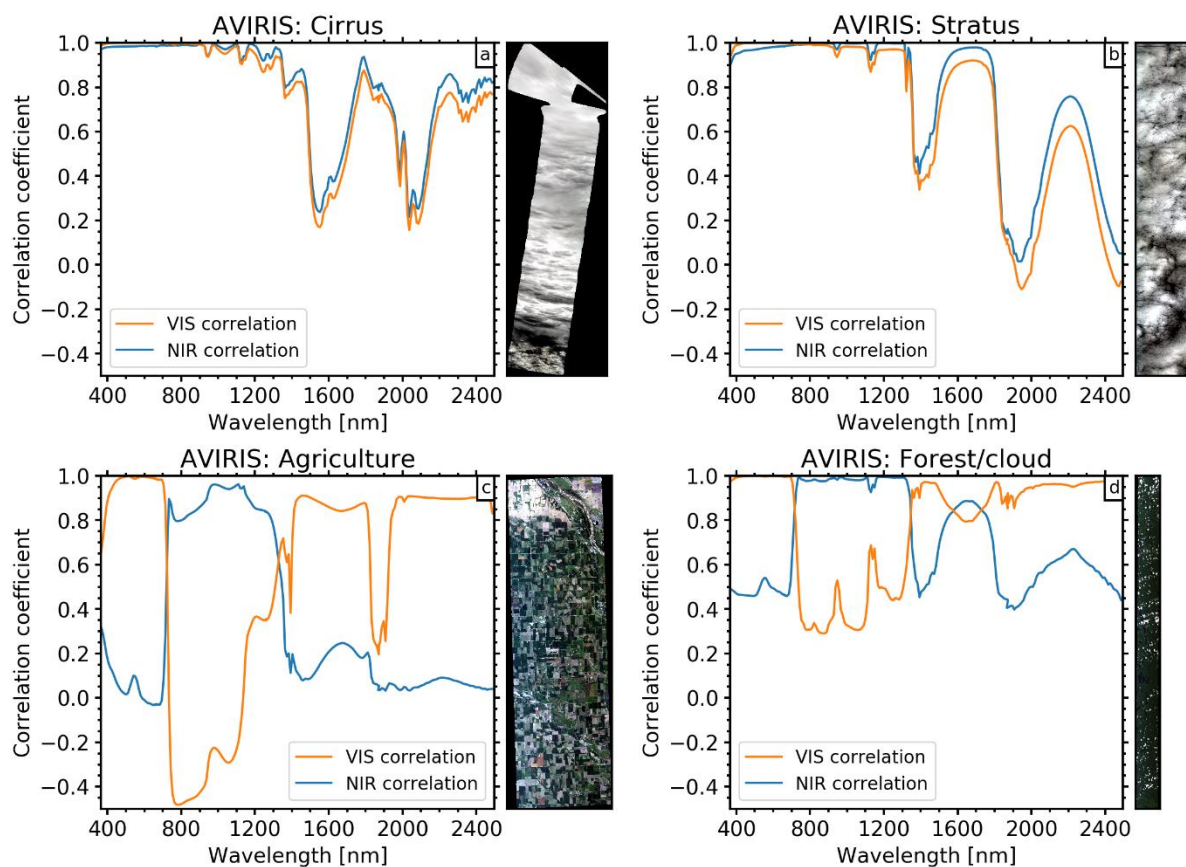
Figure 6. Pearson correlation coefficient between upwelling spectral radiances at aircraft altitude and the VIS (orange) and NIR
250 **(blue) sub-band radiances for AVIRIS scenes of (a) marine cirrus cloud, (b) marine stratocumulus cloud, (c) agriculture, and (d)**
mixed forest and cumulus clouds. The true-colour image associated with the AVIRIS observations is given to the right of each plot.

With multiple lines of evidence supporting 555 nm radiance as a reliable analogue for VIS sub-band radiance, we
proceed to stratify the globally-representative CLARREO OSSE results by scene type to gain further insights as to why.
Using the profile properties that were input to the CLARREO OSSE, we stratify scenes following the simple ERBE
255 definitions of clear sky (0-5%), partly cloudy (5-50%), mostly cloudy (50-95%), and overcast (95-100%), and surface type
categories of ocean, land, snow, and desert (henceforth "ERBE-like"; Suttles et al., 1988). When analyzing the spectral
relationships by ERBE-like scene type, we found that one of the most challenging scene types is mostly cloudy over ocean.
For this scene type, a large spread in the relationship between 865 nm and the NIR sub-band occurs, with data loosely falling
into three branches associated with changes in cloud altitude (Figure 7a). This occurs for two primary reasons: variations in
260 water vapor above clouds and cloud thermodynamic phase. While 865 nm is largely insensitive to variations in these
properties, the NIR sub band is substantially influenced by differences in water vapor, cloud liquid, and cloud ice absorption
(e.g., Gristey and Chiu, 2022; Gristey et al., 2019). Meanwhile, the same scenes exhibit very little spread in the relationship
between 555 nm and VIS (Figure 7b), as shown by the increase in the r-squared value from 0.951 to 0.996. This difference is

due to the fact that both 555 nm and VIS are largely insensitive to spectral absorption features of water in its various

265   thermodynamic phases.
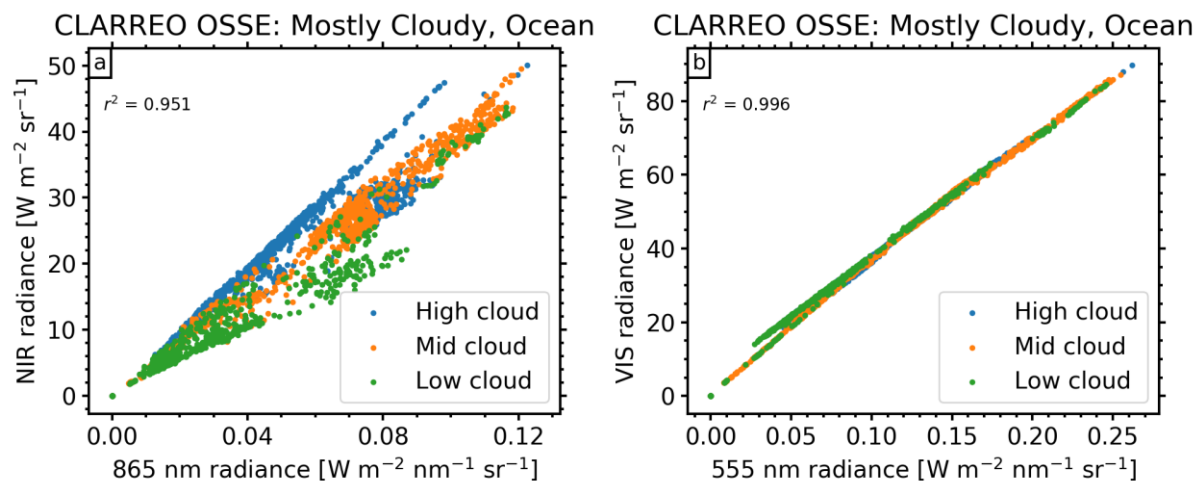
Figure 7. Relationship between nadir radiance at (a) 865 nm and the NIR sub-band, and (b) 555 nm and the VIS sub-band for mostly cloudy over ocean scenes in the CLARREO OSSE. Data points are colored as high cloud (blue), mid-level cloud (orange), or low cloud (green), defined using the International Satellite Cloud Climatology Project (ISCCP) cloud top pressure boundaries.

270   While the CLARREO OSSE has proven useful for assessing spectral relationships thus far, one of the major limitations

in the context of ADMs is that it only includes nadir radiances. It is necessary that the spectral relationships hold at nadir, but

not sufficient; since a spectral conversion is desired for angular sampling, it is also important to confirm that these results

hold at off-nadir view geometries. The SCIAMACHY observations in Figure 5b and AVIRIS observations in Figure 6

include off-nadir views providing an initial indication that solar-viewing geometry is not playing a dominant role in the

275   relationship between 555 nm and VIS radiances. A closer look with the CERES unfiltering dataset also suggests that any

dependence on geometry is relatively small (Figure 8a-c). The tight relationship between 555 nm and VIS holds across all

SZA, VZA, and RAA combinations within this dataset (only cloudy ocean scenes are shown, but the result is consistent for

other scenes within the dataset that all have r-squared values greater than 0.97). There is no obvious trend in the relationship

with SZA (Figure 8a) or RAA (Figure 8c), but there is a suggestion that limited spread in the spectral relationship is related

280   to VZA (Figure 8b), with larger VZA tending to exhibit larger VIS radiance for the same 555 nm radiance. Beyond this

qualitative statement, the dependence is difficult to quantify with the CERES unfiltering dataset given that it only includes

calculations at 5 discrete VZAs. Following the CLARREO OSSE approach, an updated and far more extensive set of

MODTRAN calculations that use finer resolution input profiles (in both space and time) and outputs radiances at fine

angular resolution across the full range of solar-viewing geometries is currently under development. This dataset will be

285   better suited to address detailed angular dependencies to implement the spectral conversion itself and quantify the associated

uncertainties, and will be the subject of a subsequent dedicated study.
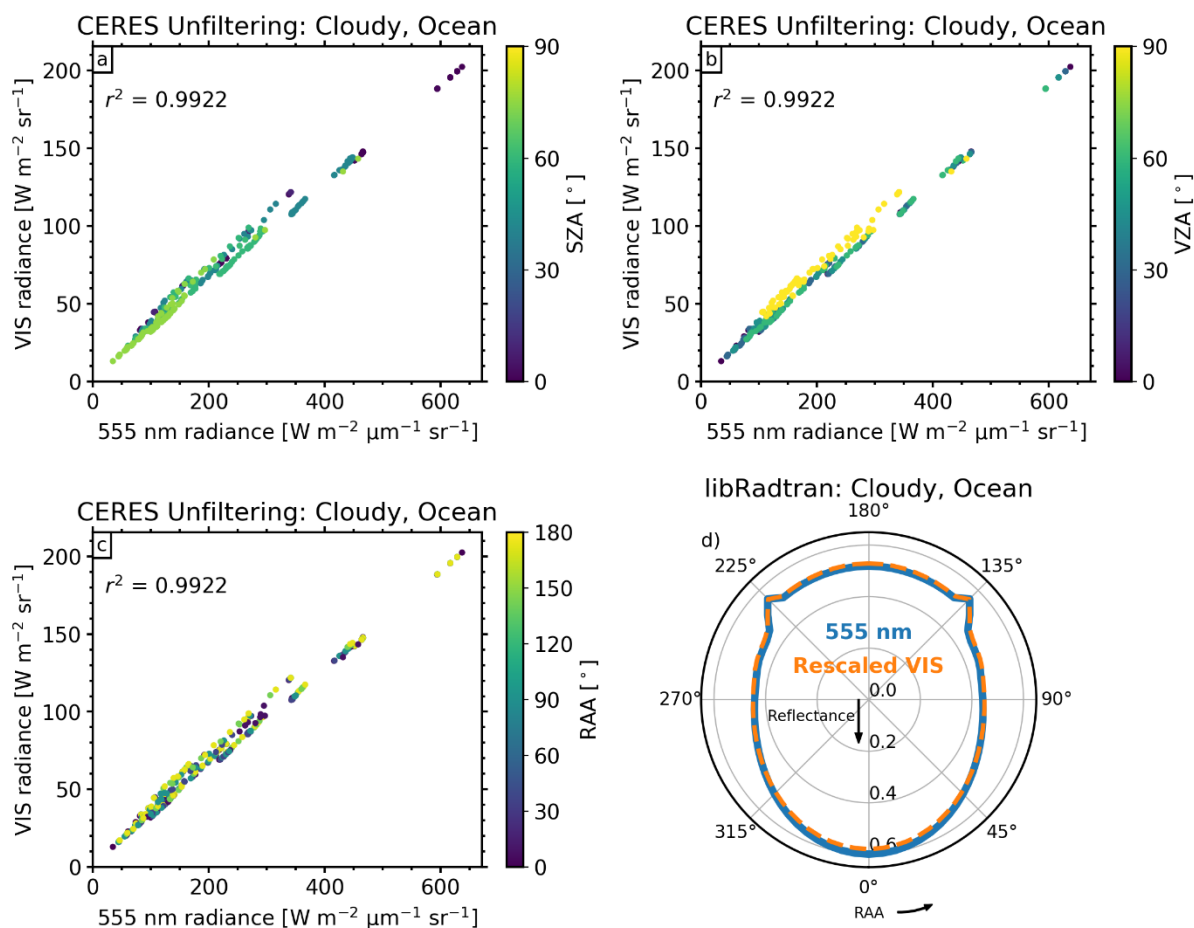
Figure 8. The relationship between 555 nm and VIS radiance in (a, b, c) the CERES unfiltering dataset for cloudy over ocean scenes with data points coloured by SZA, VZA and RAA, respectively, and in (d) the libRadtran calculation for a cloudy ocean scene at a fixed SZA (60°) and VZA (45°) showing the detailed variation in RAA.

The consistency of the relationship between 555 nm and VIS with solar-viewing geometry is further supported by a libradtran calculation of TOA reflectance over a cloudy ocean scene as an example (Figure 8d). This calculation shows that the detailed variations with relative azimuth angle follow an almost identical shape for both 555 nm and VIS, including the peak in reflectance near ±45° RAA associated with the cloud-bow. Analysis of detailed angular variations should be extended in the future to other scenes that might be more challenging such as sun-glint, but this result already builds confidence that the tight spectral relationship also holds across detailed angular features to be incorporated into ADM generation.

Another option to address the lack of observational angular sampling in the split-SW is to apply a spectral conversion from total SW to split-SW to take advantage of the extensive angular sampling already obtained from the CERES instruments (Norman Loeb, personal communication). While this approach certainly warrants further investigation, it would undoubtedly require further scene stratification during the spectral conversion because the total SW includes the NIR

spectral complexities discussed above. This could potentially be overcome by making the spectral conversion a function of properties such as the above cloud water vapor. However, these properties would then need to be retrieved for every CERES footprint, which comes with its own challenges and uncertainties. We intentionally avoid these uncertainties for now given

305   that such properties are important factors in determining where energy is deposited in the atmosphere, which is precisely what the split-SW observations can help to inform us on (Hakuba et al., 2022; Carlson et al., 2019; Collins et al., 2006).

5 Synthetic camera angular sampling

To quantify the capability of a camera to provide dense angular sampling of various scene types required for rapid ADM generation, we ran a simulation experiment to project the camera sampling onto existing satellite retrievals. Figure 9 shows an example of instantaneous camera sampling following application of the pixel masks outlined in Section 3 onto the CIRES

310   Cookie Dough data described in Section 2. By matching the ADM samples to the underlying geophysical retrievals, we can determine the scene characteristics that a camera would have observed if it were flying on an existing satellite, in this case NOAA-20. It is immediately apparent that some ADM samples fall outside the Cookie Dough data (shown in purple). This is because VIIRS does not scan all the way to the horizon, whereas a WFOV camera would capture those geometries (see

315   Figure 2). However, most ADM samples are co-located with the Cookie Dough data (shown in red), including at acute VZA in the along-track directions with a modest time offset.
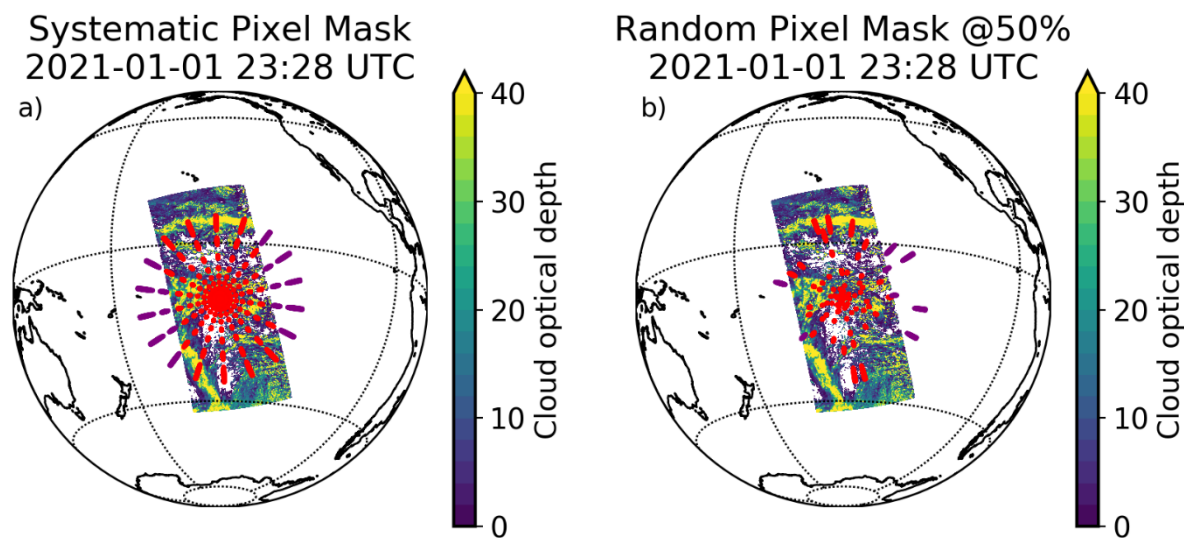
Figure 9. An example of instantaneous synthetic camera sampling over the Pacific Ocean for (a) a systematic camera pixel mask with ADM samples at the centre of every CERES-TRMM angular bin, and (b) a randomized camera pixel mask with ADM
320   **samples randomly located in only 50% of CERES-TRMM angular bins. ADM samples in red indicate that all pixels are co-located with VIIRS (retrieved cloud optical depth ± 9 min is shown in colours as an example, which covers the instantaneous WFOV), while ADM samples in purple indicate at least one pixel in the ADM sample falls outside the VIIRS swath. Snapshot is valid on 1 January 2021 at 23:28 UTC.**

For each camera pixel within an ADM sample that is co-located with the Cookie Dough, we determine the cloud fraction

325 and surface type via nearest interpolation to the co-located Cookie Dough data. The surface type provided in the Cookie

Dough is based on the International Geosphere–Biosphere Programme (IGBP) surface classification, which we map to

ERBE-like surface types using Table 2. We then calculate the surface type for an ADM sample as the mode of the pixel-

level values and the cloud fraction as the mean of the pixel-level values. This enables us to assign the ADM sample to an

ERBE-like scene type, providing an initial look at camera angular sampling stratified by scene type.

330 **Table 2. Mapping between IGBP and ERBE-like surface types. Three additional categories accounting for the variable surface in the cryosphere are added for CERES processing from the National Snow and Ice Data Center (NSIDC).**

IGBP index	IGBP surface type	ERBE surface type
1	Evergreen needle-leaf forest	Land
2	Evergreen broad-leaf forest	Land
3	Deciduous needle-leaf forest	Land
4	Deciduous broad-leaf forest	Land
5	Mixed forest	Land
6	Closed shrubland	Land
7	Open shrubland (desert)	Desert
8	Woody savanna	Land
9	Savanna	Land
10	Grassland	Land
11	Permanent wetland	Land
12	Cropland	Land
13	Urban and built-up	Land
14	Cropland/natural vegetation mosaics	Land
15	Permanent snow and ice	Snow
16	Barren (desert)	Desert
17	Water	Ocean
N/A (NSIDC)	Tundra	Land
N/A (NSIDC)	Fresh snow	Snow
N/A (NSIDC)	Sea ice	Snow

After just 23-hours of sampling with the systematic pixel mask (Figure 10, left half of plots), almost all angular bins for

all scene types are sampled. The most frequent scene types (e.g., cloudy ocean) typically have every angular bin filled with

335 hundreds-to-thousands of samples, whereas the least frequent scene types (e.g., cloudy desert) typically have around ten or

less samples in each angular bin. Only a couple of sporadic angular bins are not sampled in the outer VZA, mainly because

less ADM samples are co-located with the Cookie Dough data (see Figure 9) and therefore are not included in the counts.
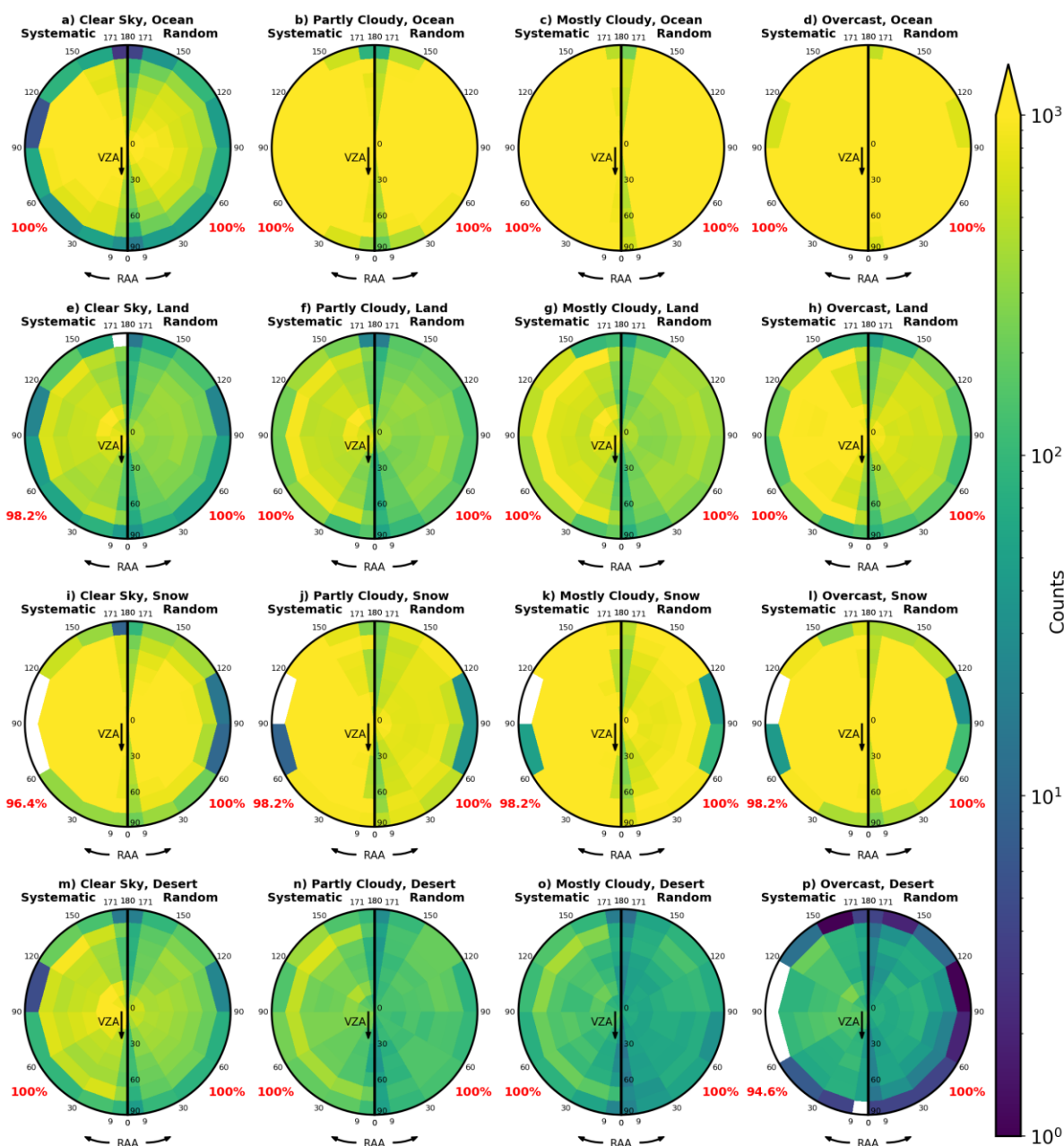
Figure 10. Number of samples in each ERBE-like angular bin and scene type after 23-hours of synthetic camera sampling. White color indicates no samples. On each plot (a–p) results from the systematic pixel mask are shown on the left, and results from the randomized pixel mask with a 50% scaling factor on the right. The percentage of angular bins filled in each case is given in red. No stratification by solar zenith angle is shown. Data from 1 January 2021.

The same 23-hours of sampling with the randomized pixel mask at a scaling factor of 50% (Figure 10, right half of plots) also provides excellent angular sampling of these scene types. Despite the overall count being reduced by half, every angular bin for every scene type contains at least one sample in this configuration. This result is broadly consistent across 3 other

simulated days spanning the annual cycle (1 Apr, 1 Jul, 1 Oct; not shown), and therefore is not dependant on the specific day chosen. Due to the improved angular coverage and the reduced data rate, the randomized pixel mask at a scaling factor of 50% is used in the remainder of this section to explore the sampling in further detail.

350   One major difference between the ERBE-like scene types applied thus far and those used in CERES products is the additional scene stratification by cloud optical depth. Since this variable is included in the Cookie Dough data, we can also look at the angular sampling as a function of cloud optical depth. For the most frequent scene type of overcast ocean (Figure 11, left half of plots), the angular sampling remains excellent within CERES-TRMM land cloud optical depth bins. However, for the least frequent scene type of overcast desert (Figure 11, right half of plots), sampling gaps start to appear. This suggests that generation of camera-based ADMs for infrequent scenes that are stratified beyond ERBE-like would

355 benefit from more than a single day of sampling. However, it is clear that ample angular sampling will be achieved in a much shorter timeframe than could otherwise be achieved by traditional RAPS sampling, likely days-to-weeks rather than months-to-years.
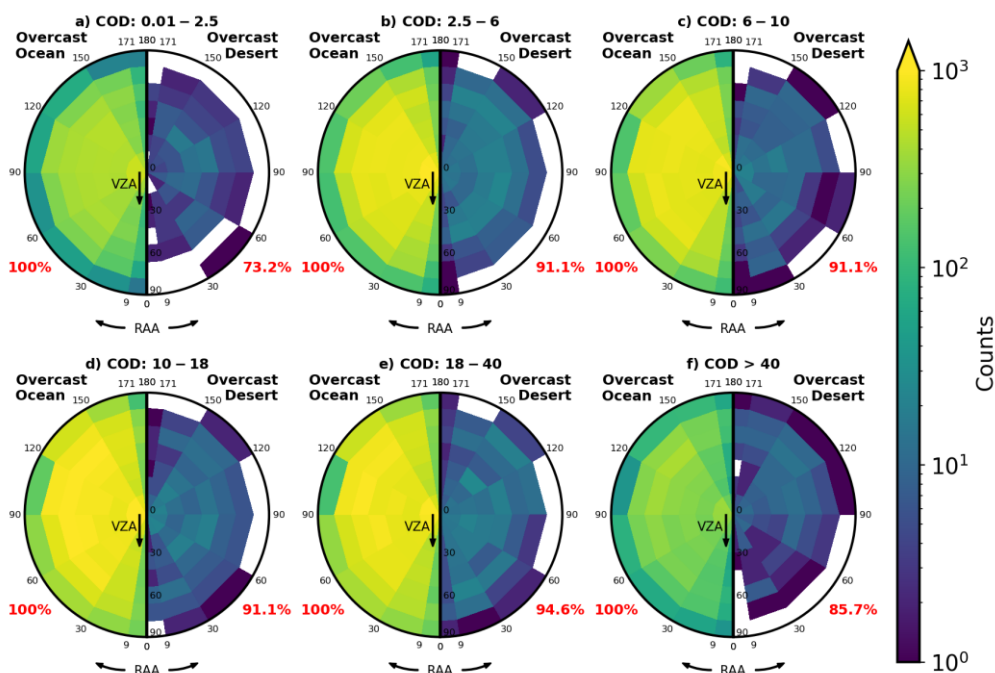
Figure 11. Number of samples in ERBE-like angular bins and scene types after 23-hours of synthetic camera sampling with the
360 **randomized pixel mask with a 50% scaling factor, additionally stratified by (a–f) CERES-TRMM cloud optical depth (COD) bins over land. White color indicates no samples. On each subplot, results are shown for the most frequent scene type of overcast ocean on the left and the least frequent scene type of overcast desert on the right. The percentage of angular bins filled in each case is given in red. Data from 1 January 2021.**

     Another dimension of ADMs not yet explored is the SZA. Figure 12 shows that angular sampling reduces with the
365 additional stratification by CERES-TRMM SZA bins, as expected. However, this does not occur monotonically as demonstrated by the two most challenging cases of snow surfaces (with the notable gaps at high sun) and desert surfaces

(with notable gaps at both high and low sun). For snow covered surfaces, this is due to their occurrence mostly at high latitudes where high sun is never encountered. For desert surfaces, this is related to the sun synchronous 13:30 equator crossing orbit of NOAA-20 that passes over the low-latitude deserts in mid-afternoon when the sun is reasonably high in the

370   sky, but not directly overhead. Unlike the other ADM dimensions, the SZA dependence exhibits a notable seasonal dependence (not shown) as Earth's declination angle varies and therefore Earth's surfaces are tilted either toward or away from the Sun. In practice, these missing angular bins can often be filled with radiative transfer calculations or directional reciprocity (di Girolamo et al., 1998; Davies, 1994; Chandrasekhar, 1960).
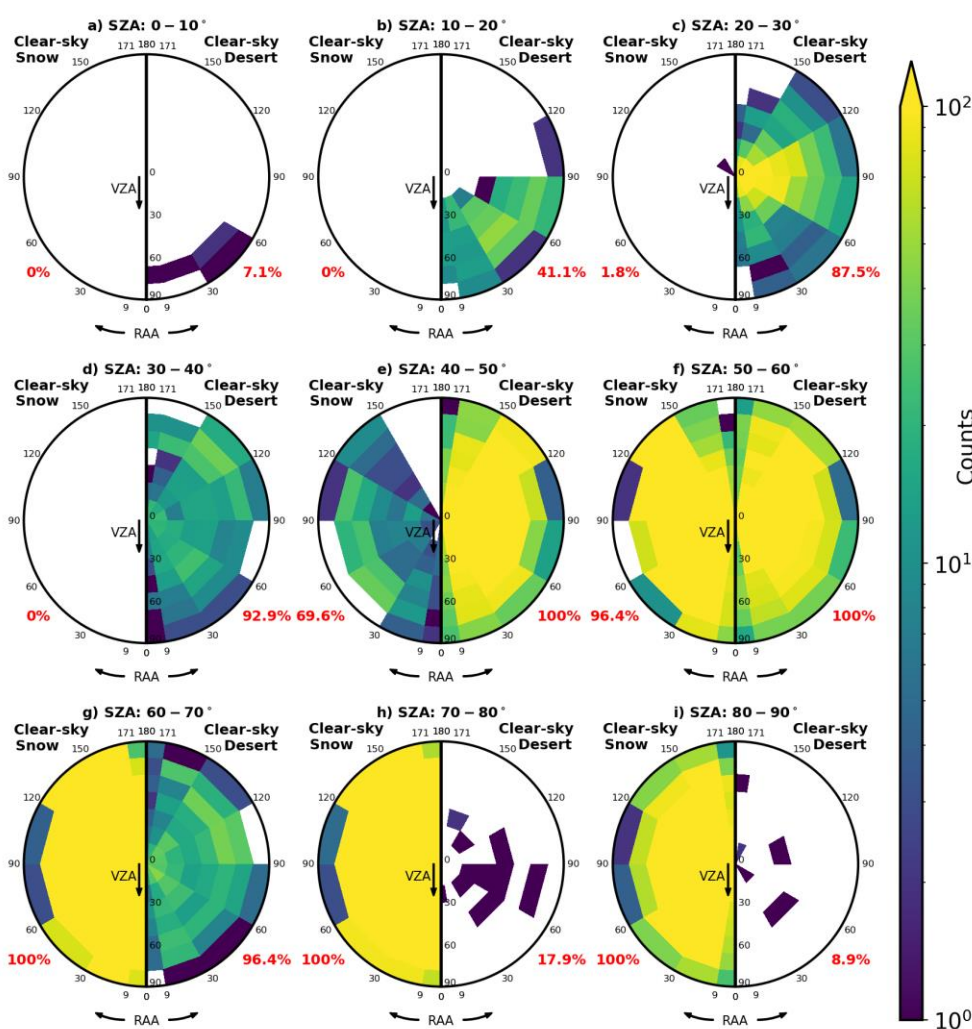
375   **Figure 12. Number of samples in ERBE-like angular bins and scene types after 23-hours of synthetic camera sampling with the randomized pixel mask with a 50% scaling factor, additionally stratified by (a–f) CERES-TRMM solar zenith angle (SZA) bins. White color indicates no samples. On each subplot, results are shown for the most challenging cases of clear-sky snow on the left and clear-sky desert on the right. The percentage of angular bins filled in each case is given in red. Data from 1 January 2021. Note that the maximum extent of the colour bar is reduced from one thousand in Figure 10 and Figure 11 to one hundred here.**

6 Summary and Conclusions

380

Satellite-based Earth radiation budget (ERB) data products depend critically on conversion of measured radiances to derived irradiances, achieved via angular distribution models (ADMs). In this study, we present the concept of a space-based camera that views the Earth from horizon-to-horizon with a large pixel array at a single wavelength to serve as a valuable resource for the generation of new ADMs. Specifically, we focus on the capability of a camera proposed to fly as part of the

385 upcoming Libera mission to provide angular sampling required to generate ADMs for the new split-SW spectral channel that Libera will host.

We start by addressing an immediate issue that arises when dealing with high-resolution camera images in space: the sheer amount of bandwidth required for frequent downlink of large arrays of pixels is operationally difficult. We note that entire camera images are not necessary for ADM generation, so we instead design a pixel mask that extracts only a small

390 subset of pixels from each image. The presented pixel mask includes multiple groups of pixels that each encompass the Libera radiometer footprint, are randomly distributed across and within the discrete CERES-TRMM angular bins, and can be scaled according to the available bandwidth. We target a 50% scaling (50% of the angular bins are sampled in each image) that extracts less than 1% of the pixels in each image.

Having extracted appropriate pixels from camera images, a spectral conversion is required to use single wavelength

395 radiances to generate split-SW ADMs. Various established and independent datasets all indicate that using a mid-visible wavelength to represent the VIS sub-band is the optimal choice, with physical reasoning supporting this choice revealed by analysing spectral relationships by scene type. Spectral relationships involving the NIR are more complicated due to variations in the spectral absorption features of water in all three thermodynamic phases, and variations in surface bi-directional reflectance. In contrast, the relationship between 555 nm and the VIS sub-band is largely insensitive to these

400 properties, requiring only basic stratification by scene type and solar-viewing geometry to generate "proxy" VIS radiances.

With proxy VIS radiances distributed across angular bins, we finally quantify how the angular bins of different scene types are sampled by projecting this camera sampling onto retrieved scene properties from the existing NOAA-20 satellite. After less than a day of sampling, ERBE-like scene types and angular bins are found to be exceptionally well sampled, with every VZA and RAA bin of every scene type receiving at least one sample, and in most cases many more. Some unavoidable

405 gaps remain in the SZA dimension, and additional stratification by cloud optical depth leads to some unsampled angular bins for infrequent scene types within this short timeframe.

While this study demonstrates the potential of a camera to augment existing ERB approaches, there are caveats that need mentioning. The presented pixel masks work well but are not necessarily optimal and could be refined further. The spectral conversion between 555 nm and VIS needs to be implemented, with a closer look at the angular dependencies; a new

410 product is under development for this purpose and will be the focus of a subsequent study. Likewise, the synthetic angular sampling could be extended to a longer-duration dataset, which would more precisely quantify the timescale required to generate ADMs similar to current CERES SW ADMs that are substantially more stratified. More broadly, ADM generation

is only one benefit that needs to be balanced with other potential ERB applications of a camera. We stress that camera-based ADMs for the Libera split-SW channels are intended as a demonstration, and sit within a wider Libera split-SW ADM

415 approach that will ultimately be constrained and tested with RAPS observations from the split-SW radiometers.

In summary, split-SW ADM generation for either ERBE-like scene types or more stratified scenes types will be possible in a substantially shorter timeframe than that from existing approaches if radiances from a monochromatic camera are used: days–weeks rather than months–years. This result can pave the way for the development of shortwave irradiance products across arbitrary sets of spectral bands through the use of monochromatic or polychromatic cameras with judiciously-chosen,

420 high-correlation wavelengths.

Data Availability

All datasets used in this study have been made available at https://csl.noaa.gov/groups/csl9/datasets/data/cloud_phys/2023-Gristey-etal/.

Author Contribution

425 J.J.G. and K.S.S. conceived and designed the study with input from all authors. J.J.G. wrote the manuscript and created all final figures. D.R.F. produced the CLARREO OSSE, B.C.K. selected and retrieved the AVIRIS data for Figure 6, J.M. provided the analysis for Figure 8a–c, and H.C. provided the analysis for Figure 8d. The manuscript received substantial editing from all authors.

Competing Interests

430 K.S.S. is a member of the editorial board of Atmospheric Measurement Techniques. The peer-review process was guided by an independent editor, and the authors have no other competing interests to declare.

Acknowledgments

This work was supported by the Earth Venture Continuity 1 (EVC-1): Libera project under NASA Contract 80LARC20D0006. J.J.G. acknowledges support from the NOAA Cooperative Agreement with CIRES, NA22OAR4320151.
435 The authors thank the CERES science team, specifically Walter Miller, Kathleen Dejwakh, and Norman Loeb for their open sharing and guidance of CERES datasets.

References

Barkstrom, B. R.: The Earth Radiation Budget Experiment (ERBE), Bull Am Meteorol Soc, 65, 1170–1185, https://doi.org/10.1175/1520-0477(1984)065<1170:TERBE>2.0.CO;2, 1984.

440   Béland, S., Harder, J., and Woods, T.: Eleven years of tracking the SORCE SIM instrument degradation caused by space radiation and solar exposure, 91434W, https://doi.org/10.1117/12.2057385, 2014.

Berk, A., Conforti, P., Kennett, R., Perkins, T., Hawes, F., and van den Bosch, J.: MODTRAN® 6: A major upgrade of the MODTRAN® radiative transfer code, Workshop on Hyperspectral Image and Signal Processing, Evolution in Remote Sensing, 2014-June, https://doi.org/10.1109/WHISPERS.2014.8077573, 2014.

445   Carlson, B., Lacis, A., Colose, C., Marshak, A., Su, W., and Lorentz, S.: Spectral Signature of the Biosphere: NISTAR Finds It in Our Solar System From the Lagrangian L-1 Point, Geophys Res Lett, 46, 10679–10686, https://doi.org/10.1029/2019GL083736, 2019.

Ceppi, P. and Nowack, P.: Observational evidence that cloud feedback amplifies global warming, Proc Natl Acad Sci U S A, 118, e2026290118, https://doi.org/10.1073/PNAS.2026290118/SUPPL_FILE/PNAS.2026290118.SAPP.PDF, 2021.

450   Cesana, G. v. and del Genio, A. D.: Observational constraint on cloud feedbacks suggests moderate climate sensitivity, Nature Climate Change 2021 11:3, 11, 213–218, https://doi.org/10.1038/s41558-020-00970-y, 2021.

Chandrasekhar, S.: Radiative Transfer, Dover Publications, 416 pp., 1960.

Chen, H., Schmidt, S., Massie, S. T., Nataraja, V., Norgren, M. S., Gristey, J. J., Feingold, G., Holz, R. E., and Iwabuchi, H.: The Education and Research 3D Radiative Transfer Toolbox (EaR3T) – Towards the Mitigation of 3D Bias in Airborne and
455   Spaceborne Passive Imagery Cloud Retrievals, Atmospheric Measurement Techniques Discussion, https://doi.org/https://doi.org/10.5194/amt-2022-143, 2022.

Collins, W. D., Lee-Taylor, J. M., Edwards, D. P., and Francis, G. L.: Effects of increased near-infrared absorption by water vapor on the climate system, Journal of Geophysical Research: Atmospheres, 111, 18109, https://doi.org/10.1029/2005JD006796, 2006.

460   Corbett, J. and Su, W.: Accounting for the effects of sastrugi in the CERES clear-sky Antarctic shortwave angular distribution models, Atmos Meas Tech, 8, 3163–3175, https://doi.org/10.5194/amt-8-3163-2015, 2015.

Davies, R.: Spatial autocorrelation of radiation measured by the Earth Radiation Budget Experiment: Scene inhomogeneity and reciprocity violation, J Geophys Res, 99, https://doi.org/10.1029/94JD01680, 1994.

Diner, D. J., Beckert, J. C., Reilly, T. H., Bruegge, C. J., Conel, J. E., Kahn, R. A., Martonchik, J. v., Ackerman, T. P.,
465   Davies, R., Gerstl, S. A. W., Gordon, H. R., Muller, J. P., Myneni, R. B., Sellers, P. J., Pinty, B., and Verstraete, M. M.: Multi-angle imaging spectroradiometer (MISR) instrument description and experiment overview, IEEE Transactions on Geoscience and Remote Sensing, 36, 1072–1087, https://doi.org/10.1109/36.700992, 1998.

Emde, C., Buras-Schnell, R., Kylling, A., Mayer, B., Gasteiger, J., Hamann, U., Kylling, J., Richter, B., Pause, C., Dowling, T., and Bugliaro, L.: The libRadtran software package for radiative transfer calculations (version 2.0.1), Geosci. Model Dev, 9, 1647–1672, https://doi.org/10.5194/gmd-9-1647-2016, 2016.

Feldman, D. R., Algieri, C. A., Ong, J. R., and Collins, W. D.: CLARREO shortwave observing system simulation experiments of the twenty-first century: Simulator design and implementation, J Geophys Res, 116, D10107, https://doi.org/10.1029/2010JD015350, 2011a.

Feldman, D. R., Algieri, C. A., Collins, W. D., Roberts, Y. L., and Pilewski, P. A.: Simulation studies for the detection of changes in broadband albedo and shortwave nadir reflectance spectra under a climate change scenario, Journal of Geophysical Research: Atmospheres, 116, D24103, https://doi.org/10.1029/2011JD016407, 2011b.

Feldman, D. R., Collins, W. D., and Paige, J. L.: Pan-spectral observing system simulation experiments of shortwave reflectance and long-wave radiance for climate model evaluation, Geosci Model Dev, 8, 1943–1954, https://doi.org/10.5194/gmd-8-1943-2015, 2015.

Forster, P. M. F. and Gregory, J. M.: The Climate Sensitivity and Its Components Diagnosed from Earth Radiation Budget Data, J Clim, 19, 39–52, https://doi.org/10.1175/JCLI3611.1, 2006.

di Girolamo, L., Várnai, T., and Davies, R.: Apparent breakdown of reciprocity in reflected solar radiances, Journal of Geophysical Research: Atmospheres, 103, 8795–8803, https://doi.org/10.1029/98JD00345, 1998.

Gottwald, M. and Bovensmann, H. (Eds.): SCIAMACHY - Exploring the Changing Earth's Atmosphere, Springer Netherlands, Dordrecht, https://doi.org/10.1007/978-90-481-9896-2, 2011.

Green, R. O., Eastwood, M. L., Sarture, C. M., Chrien, T. G., Aronsson, M., Chippendale, B. J., Faust, J. A., Pavri, B. E., Chovit, C. J., Solis, M., Olah, M. R., and Williams, O.: Imaging Spectroscopy and the Airborne Visible/Infrared Imaging Spectrometer (AVIRIS), Remote Sens Environ, 65, 227–248, https://doi.org/10.1016/S0034-4257(98)00064-9, 1998.

Gristey, J. J. and Chiu, J. C.: Understanding our Climate System through the Lens of Spectral Reflected Solar Radiation, in: International Radiation Symposium, 2022.

Gristey, J. J., Christine Chiu, J., Gurney, R. J., Shine, K. P., Havemann, S., Thelen, J. C., and Hill, P. G.: Shortwave Spectral Radiative Signatures and Their Physical Controls, J Clim, 32, 4805–4828, https://doi.org/10.1175/JCLI-D-18-0815.1, 2019.

Gristey, J. J., Su, W., Loeb, N. G., Vonder Haar, T. H., Tornow, F., Schmidt, K. S., Hakuba, M. Z., Pilewskie, P., and Russell, J. E.: Shortwave Radiance to Irradiance Conversion for Earth Radiation Budget Satellite Observations: A Review, Remote Sensing 2021, Vol. 13, Page 2640, 13, 2640, https://doi.org/10.3390/RS13132640, 2021.

Hakuba, M. Z., Kindel, B., Gristey, J. J., Bodas-Salcedo, A., Stephens, G., and Pilewskie, P.: Simulated variability in visible and near-IR irradiances in preparation for the upcoming Libera mission, in: International Radiation Symposium, 2022.

Harries, J. E., Russell, J. E., Hanafin, J. A., Brindley, H., Futyan, J., Rufus, J., Kellock, S., Matthews, G., Wrigley, R., Last, A., Mueller, J., Mossavati, R., Ashmall, J., Sawyer, E., Parker, D., Caldwell, M., Allan, P. M., Smith, A., Bates, M. J., Coan, B., Stewart, B. C., Lepine, D. R., Cornwall, L. A., Corney, D. R., Ricketts, M. J., Drummond, D., Smart, D., Cutler, R., Dewitte, S., Clerbaux, N., Gonzalez, L., Ipe, A., Bertrand, C., Joukoff, A., Crommelynck, D., Nelms, N., Llewellyn-Jones,

D. T., Butcher, G., Smith, G. L., Szewczyk, Z. P., Mlynczak, P. E., Slingo, A., Allan, R. P., and Ringer, M. A.: The Geostationary Earth Radiation Budget Project, Bull Am Meteorol Soc, 86, 945–960, https://doi.org/10.1175/BAMS-86-7-945, 2005.

505   Hartmann, D. L. and Ceppi, P.: Trends in the CERES Dataset, 2000–13: The Effects of Sea Ice and Jet Shifts and Comparison to Climate Models, J Clim, 27, 2444–2456, https://doi.org/10.1175/JCLI-D-13-00411.1, 2014.

Havemann, S., Thelen, J.-C., Taylor, J. P., and Harlow, R. C.: The Havemann-Taylor Fast Radiative Transfer Code (HT-FRTC): A multipurpose code based on principal components, J Quant Spectrosc Radiat Transf, 220, 180–192, https://doi.org/10.1016/J.JQSRT.2018.09.008, 2018.

510   Jacobowitz, H., Soule, H. V., Kyle, H. L., and House, F. B.: The Earth Radiation Budget (ERB) Experiment: An overview, Journal of Geophysical Research: Atmospheres, 89, 5021–5038, https://doi.org/10.1029/JD089iD04p05021, 1984.

Kandel, R., Viollier, M., Raberanto, P., Duvel, J. P., Pakhomov, L. A., Golovko, V. A., Trishchenko, A. P., Mueller, J., Raschke, E., Stuhlmann, R. R., and Scientific Working Group (ISSWG), I. S. R. B.: The ScaRaB Earth Radiation Budget Dataset, Bull Am Meteorol Soc, 79, 765–783, https://doi.org/10.1175/1520-0477(1998)079<0765:TSERBD>2.0.CO;2,

515   1998.

Kramer, R. J., He, H., Soden, B. J., Oreopoulos, L., Myhre, G., Forster, P. M., and Smith, C. J.: Observational Evidence of Increasing Global Radiative Forcing, Geophys Res Lett, 48, e2020GL091585, https://doi.org/10.1029/2020GL091585, 2021.

Kyle, H. L., Arking, A., Hickey, J. R., Ardanuy, P. E., Jacobowitz, H., Stowe, L. L., Campbell, G. G., Vonder Haar, T., House, F. B., Maschhoff, R., and Smith, G. L.: The Nimbus Earth Radiation Budget (ERB) Experiment: 1975 to 1992, Bull

520   Am Meteorol Soc, 74, 815–830, https://doi.org/10.1175/1520-0477(1993)074<0815:TNERBE>2.0.CO;2, 1993.

Loeb, N. G. and Wielicki, B. A.: Satellites and Satellite Remote Sensing: Earth's Radiation Budget, in: Encyclopedia of Atmospheric Sciences: Second Edition, Elsevier Inc., 67–76, https://doi.org/10.1016/B978-0-12-382225-3.00349-2, 2015.

Loeb, N. G., Priestley, K. J., Kratz, D. P., Geier, E. B., Green, R. N., Wielicki, B. A., Hinton, P. O., and Nolan, S. K.: Determination of Unfiltered Radiances from the Clouds and the Earth's Radiant Energy System Instrument, Journal of

525   Applied Meteorology, 40, 822–835, https://doi.org/10.1175/1520-0450(2001)040<0822:DOURFT>2.0.CO;2, 2001.

Loeb, N. G., Manalo-Smith, N., Kato, S., Miller, W. F., Gupta, S. K., Minnis, P., and Wielicki, B. A.: Angular Distribution Models for Top-of-Atmosphere Radiative Flux Estimation from the Clouds and the Earth's Radiant Energy System Instrument on the Tropical Rainfall Measuring Mission Satellite. Part I: Methodology, Journal of Applied Meteorology, 42, 240–265, https://doi.org/10.1175/1520-0450(2003)042<0240:ADMFTO>2.0.CO;2, 2003a.

530   Loeb, N. G., Loukachine, K., Manalo-Smith, N., Wielicki, B. A., and Young, D. F.: Angular distribution models for top-of tmosphere radiative flux estimation from the clouds and the Earth's Radiant Energy system instrument on the Tropical Rainfall Measuring Mission satellite. Part II: Validation, Journal of Applied Meteorology, 42, 1748–1769, https://doi.org/10.1175/1520-0450(2003)042<1748:ADMFTR>2.0.CO;2, 2003b.

Loeb, N. G., Kato, S., Loukachine, K., and Manalo-Smith, N.: Angular Distribution Models for Top-of-Atmosphere

535 Radiative Flux Estimation from the Clouds and the Earth's Radiant Energy System Instrument on the *Terra* Satellite. Part I: Methodology, J Atmos Ocean Technol, 22, 338–351, https://doi.org/10.1175/JTECH1712.1, 2005.

Loeb, N. G., Kato, S., Loukachine, K., Manalo-Smith, N., and Doelling, D. R.: Angular distribution models for top-of-atmosphere radiative flux estimation from the Clouds and the Earth's Radiant Energy System instrument on the Terra Satellite. Part II: Validation, J Atmos Ocean Technol, 24, 564–584, https://doi.org/10.1175/JTECH1983.1, 2007.

540 Mayer, B. and Kylling, A.: Technical note: The libRadtran software package for radiative transfer calculations - Description and examples of use, Atmos Chem Phys, 5, 1855–1877, https://doi.org/10.5194/ACP-5-1855-2005, 2005.

Minnis, P., Sun-Mack, S., Chen, Y., Chang, F. L., Yost, C. R., Smith, W. L., Heck, P. W., Arduini, R. F., Bedka, S. T., Yi, Y., Hong, G., Jin, Z., Painemal, D., Palikonda, R., Scarino, B. R., Spangenberg, D. A., Smith, R. A., Trepte, Q. Z., Yang, P., and Xie, Y.: CERES MODIS Cloud Product Retrievals for Edition 4 - Part I: Algorithm Changes, IEEE Transactions on

545 Geoscience and Remote Sensing, 59, 2744–2780, https://doi.org/10.1109/TGRS.2020.3008866, 2021.

Myers, T. A., Scott, R. C., Zelinka, M. D., Klein, S. A., Norris, J. R., and Caldwell, P. M.: Observational constraints on low cloud feedback reduce uncertainty of climate sensitivity, Nat Clim Chang, 11, 501–507, https://doi.org/10.1038/s41558-021-01039-0, 2021.

Raghuraman, S. P., Paynter, D., and Ramaswamy, V.: Anthropogenic forcing and response yield observed positive trend in

550 Earth's energy imbalance, Nature Communications 2021 12:1, 12, 1–10, https://doi.org/10.1038/s41467-021-24544-4, 2021.

Raschke, E. and Bandeen, W. R.: The Radiation Balance of the Planet Earth from Radiation Measurements of the Satellite Nimbus II, Journal of Applied Meteorology, 9, 215–238, https://doi.org/10.1175/1520-0450(1970)009<0215:trbotp>2.0.co;2, 1970.

Raschke, E., Vonder Haar, T. H., Bandeen, W. R., and Pasternak, M.: The Annual Radiation Balance of the Earth-

555 Atmosphere System During 1969–70 from Nimbus 3 Measurements, J Atmos Sci, 30, 341–364, https://doi.org/10.1175/1520-0469(1973)030<0341:TARBOT>2.0.CO;2, 1973.

Stephens, G. L., Li, J., Wild, M., Clayson, C. A., Loeb, N., Kato, S., L'Ecuyer, T., Stackhouse, P. W., Lebsock, M., and Andrews, T.: An update on Earth's energy balance in light of the latest global observations, Nat Geosci, 5, 691–696, https://doi.org/10.1038/ngeo1580, 2012.

560 Suttles, J., Green, R., Minnis, P., Smith, G., Staylor, W., Wielicki, B., Walker, I., Young, D., Taylor, V., and Stowe, L.: Angular Radiation Models for Earth-Atmosphere Systems, Vol. I Shortwave Radiation, Hampton, 1988.

Su, W., Corbett, J., Eitzen, Z., and Liang, L.: Next-generation angular distribution models for top-of-atmosphere radiative flux calculation from CERES instruments: methodology, Atmos Meas Tech, 8, 611–632, https://doi.org/10.5194/amt-8-611-2015, 2015a.

565 Su, W., Corbett, J., Eitzen, Z., and Liang, L.: Next-generation angular distribution models for top-of-atmosphere radiative flux calculation from CERES instruments: Validation, Atmos Meas Tech, 8, 3297–3313, https://doi.org/10.5194/amt-8-3297-2015, 2015b.

Tett, S. F. B., Rowlands, D. J., Mineter, M. J., and Cartis, C.: Can Top-of-Atmosphere Radiation Measurements Constrain Climate Predictions? Part II: Climate Sensitivity, J Clim, 26, 9367–9383, https://doi.org/10.1175/JCLI-D-12-00596.1, 2013a.

570 Tett, S. F. B., Mineter, M. J., Cartis, C., Rowlands, D. J., and Liu, P.: Can Top-of-Atmosphere Radiation Measurements Constrain Climate Predictions? Part I: Tuning, J Clim, 26, 9348–9366, https://doi.org/10.1175/JCLI-D-12-00595.1, 2013b.

Trenberth, K. E.: An imperative for climate change planning: tracking Earth's global energy, Curr Opin Environ Sustain, 1, 19–27, https://doi.org/10.1016/j.cosust.2009.06.001, 2009.

Trepte, Q. Z., Minnis, P., Sun-Mack, S., Yost, C. R., Chen, Y., Jin, Z., Hong, G., Chang, F. L., Smith, W. L., Bedka, K. M.,

575 and Chee, T. L.: Global Cloud Detection for CERES Edition 4 Using Terra and Aqua MODIS Data, IEEE Transactions on Geoscience and Remote Sensing, 57, 9410–9449, https://doi.org/10.1109/TGRS.2019.2926620, 2019.

Vonder Haar, T. H. and Suomi, V. E.: Measurements of the Earth's Radiation Budget from Satellites During a Five-Year Period. Part I: Extended Time and Space Means, J Atmos Sci, 28, 305–314, https://doi.org/10.1175/1520-0469(1971)028<0305:MOTERB>2.0.CO;2, 1971.

580 Wielicki, B. A., Barkstrom, B. R., Harrison, E. F., Lee, R. B., Louis Smith, G., and Cooper, J. E.: Clouds and the Earth's Radiant Energy System (CERES): An Earth Observing System Experiment, Bull Am Meteorol Soc, 77, 853–868, https://doi.org/10.1175/1520-0477(1996)077<0853:CATERE>2.0.CO;2, 1996.

Wielicki, B. A., Young, D. F., Mlynczak, M. G., Thome, K. J., Leroy, S., Corliss, J., Anderson, J. G., Ao, C. O., Bantges, R., Best, F., Bowman, K., Brindley, H., Butler, J. J., Collins, W., Dykema, J. A., Doelling, D. R., Feldman, D. R., Fox, N.,

585 Huang, X., Holz, R., Huang, Y., Jin, Z., Jennings, D., Johnson, D. G., Jucks, K., Kato, S., Kirk-Davidoff, D. B., Knuteson, R., Kopp, G., Kratz, D. P., Liu, X., Lukashin, C., Mannucci, A. J., Phojanamongkolkij, N., Pilewskie, P., Ramaswamy, V., Revercomb, H., Rice, J., Roberts, Y., Roithmayr, C. M., Rose, F., Sandford, S., Shirley, E. L., Smith, W. L., Soden, B., Speth, P. W., Sun, W., Taylor, P. C., Tobin, D., and Xiong, X.: Achieving Climate Change Absolute Accuracy in Orbit, Bull Am Meteorol Soc, 94, 1519–1539, https://doi.org/10.1175/BAMS-D-12-00149.1, 2013.

590 Wild, M., Folini, D., Hakuba, M. Z., Schär, C., Seneviratne, S. I., Kato, S., Rutan, D., Ammann, C., Wood, E. F., and König-Langlo, G.: The energy balance over land and oceans: an assessment based on direct observations and CMIP5 climate models, Clim Dyn, 44, 3393–3429, https://doi.org/10.1007/s00382-014-2430-z, 2015.